Molecular Therapy
Methods & Clinical Development
Original Article

Structural basis for the neurotropic AAV9 and the engineered AAVPHP.eB recognition with cellular receptors

Guangxue Xu,[1,6] Ran Zhang,[1,2,6] Huapeng Li,[3] Kaixin Yin,[4] Xinyi Ma,[5] and Zhiyong Lou[1]

[1]MOE Key Laboratory of Protein Science & Collaborative Innovation Center of Biotherapy, School of Medicine, Tsinghua University, Beijing, China; [2]School of Life Sciences, Tsinghua University, Beijing, China; [3]PackGene Biotech, Guangzhou, Guangdong, China; [4]International School of Beijing, Beijing, China; [5]Beijing No.8 High School, Beijing, China

Clade F adeno-associated virus (AAV) 9 has been utilized as therapeutic gene delivery vector, and it is capable of crossing blood brain barrier (BBB). Recently, an AAV9-based engineering serotype AAVPHP.eB with enhanced BBB crossing ability further expanded clade F AAVs' usages in the murine central nervous system (CNS) gene delivery. In this study, we determined the cryo-electron microscopy (cryo-EM) structures of the AAVPHP.eB and its parental serotype AAV9 in native form or in complex with their essential receptor AAV receptor (AAVR). These structures reveal the molecular details of their AAVR recognition, where the polycystic kidney disease repeat domain 2 (PKD2) of AAVR interacts with AAV9 and AAVPHP.eB virions at the 3-fold protrusions and the raised capsid regions between the 2- and 5-fold axes, termed the 2/5-fold wall. The interacting patterns of AAVR to AAV9 and AAVPHP.eB are similar to what was observed in AAV1/AAV2-AAVR complexes. Moreover, we found that the AAVPHP.eB variable region VIII (VR-VIII) may independently facilitate the new receptor recognition responsible for enhanced CNS transduction. Our study provides insights into the recognition principles of multiple receptors for engineered AAVPHP.eB and parental serotype AAV9, and further reveal the potential molecular basis underlying their different tropisms.

INTRODUCTION

Gene therapy offers a promising therapeutic approach for genetic disorders. With the rapid development of gene delivery vectors, delivery method plays a crucial role in gene therapy. Among various gene therapy delivery vectors, adeno-associated viruses (AAVs) fulfill the criteria for being highly efficient and non-pathogenic as viral vectors in the human body. To date, there have been several US Food and Drug Administration (FDA)-approved AAV-based gene therapies, and numerous ongoing clinical trials.[1–3]

Naturally occurring serotypes of AAVs have been demonstrated to have varied tropisms and transduction efficiencies in tissues;[4] however, therapeutic delivery through the blood brain barrier (BBB) remains a challenge for the application of gene therapy in neurological disorders.[5] Several *in vivo*-selected AAV capsids derived from AAV9, such as AAVPHP.eB and AAVPHP.V1, have shown their enhanced BBB-penetrating ability in particular mouse strains via intravenous administration.[6–8] But the underlying mechanisms for the BBB crossing of these serotypes remain unclear. AAV receptor (AAVR) is a transmembrane glycosylated protein containing five polycystic kidney disease (PKD) extracellular domains.[9] AAVR is reported to likely play a role in AAV tropism, and AAVs adopt distinct interaction patterns to different PKD domains of AAVR.[10,11] With the assistance of bioinformatic approaches, recent studies have also identified a glycosylphosphatidylinositol (GPI)-anchored protein expressed on brain endothelial cells, called lymphocyte antigen 6 complex, locus A (LY6A, also known as stem cell antigen-1 [SCA-1]), to be the cellular receptor responsible for the enhanced AAVPHP.eB movement across BBB.[12,13]

In this study, we report the cryo-electron microscopy (cryo-EM) structure of engineered AAVPHP.eB and its parental serotype AAV9 as well as their complexes with the universal AAVR. We found minor differences in interaction pattern of AAV9/PHP.eB to AAVR compared with AAV1 and AAV2, and engineered VR-VIII in AAVPHP.eB did not participate in AAVR interaction. We then further explored the interaction between AAVPHP.eB and recently identified receptor LY6A. The preliminary structure of AAVPHP.eB with LY6A indicated that the seven-amino-acid (TLAVPFK) insertion in AAV capsid variable region VIII (VR-VIII) has potential interaction directly with LY6A. This structural finding could further reveal the underlying molecular basis of AAVPHP.eB interaction with new receptor LY6A responsible for enhanced BBB penetration and CNS transduction, and provide molecular insights into AAV vector engineering.

Received 18 September 2021; accepted 25 May 2022;
https://doi.org/10.1016/j.omtm.2022.05.009.

[6]These authors contribute equally

Correspondence: Guangxue Xu, MOE Key Laboratory of Protein Science & Collaborative Innovation Center of Biotherapy, School of Medicine, Tsinghua University, Beijing, China.
E-mail: xgx16@tsinghua.org.cn
Correspondence: Zhiyong Lou, MOE Key Laboratory of Protein Science & Collaborative Innovation Center of Biotherapy, School of Medicine, Tsinghua University, Beijing, China.
E-mail: louzy@mail.tsinghua.edu.cn

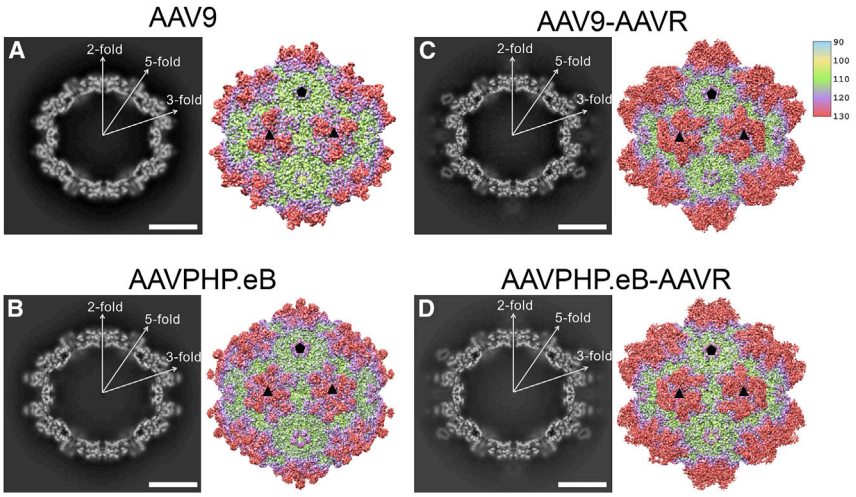

Figure 1. Cryo-EM reconstruction of AAV9 and AAVPHP.eB particles with or without AAVR binding

(A) AAV9, (B) AAVPHP.eB, (C) AAV9-AAVR, and (D) AAVPHP.eB-AAVR. The central cross sections are shown with the icosahedral 2-, 3-, and 5-fold axes. Density maps are radially colored by distance as shown in the color key. Icosahedral 3-fold axis and 5-fold axis are represented by black triangles and pentagons, respectively. The scale bars represent 100 Å.

RESULTS

Overall structures of AAV9 and AAV-PHP.eB in their native form and AAVR bounded form

We solved the structures of native AAV9 and AAV-PHP.eB by cryo-EM at the resolution of 3.87 Å and 2.85 Å at a 0.143 cutoff of Fourier Shell Correlation (FSC) (Table S1; Figures S1 and S2). AAV9 and AAVPHP.eB share common structural features with reported AAV9 crystal and cryo-EM structure and other structures of AAV serotypes,[14,15] including protrusions surrounding the 3-fold axes, a channel-like structure at 5-fold axes, and depressions at the icosahedral 2-fold axes. A 2/5-fold wall is located between the depression at the 2-fold axis and the 5-fold channel. (Figures 1A and 1B). More pronounced protrusions around the 3-fold axis were observed in AAVPHP.eB capsid compared with those in AAV9 capsid (Figure 1B).

Next, AAV9 and AAVPHP.eB were individually incubated with the soluble AAVR extracellular fragment containing PKD1-5, and structures of the AAV9-AAVR and AAVPHP.eB-AAVR complexes were subsequently determined by cryo-EM. The final resolutions of the cryo-EM reconstruction were estimated to be 3.23 Å for the AAV9-AAVR complex and 3.76 Å for the AAVPHP.eB-AAVR complex at a 0.143 cutoff of FSC (Table S1; Figure S1). The resolution of additional attached density sitting above AAV9 and AAVPHP.eB capsid in AAVR complex reconstructions were sufficient to be identified as AAVR PKD2 (Figure S3). The AAVR PKD2 interacts with AAV9 or AAVPHP.eB capsid at the 3-fold protrusions and the 2/5-fold wall, which share similar AAVR interaction pattern in AAV1 and AAV2 (Figure 2).[11,16,17]

AAV9 and AAVPHP.eB receptor binding interfaces

Resembling the engagement pattern of AAVR with AAV1 and AAV2, one PKD2 molecule also interacts with two capsid proteins of AAV9 or AAVPHP.eB (Figure 2). A total of 19 AAVR residues were within 4 Å distance of the AAV9 capsid and a total of 20 AAVR residues were within 4 Å distance of the AAVPHP.eB capsid (Table S2 and S3). Most AAV9 capsid interacting residues of PKD2 reside in the N-terminal, A-B loop and B-C loop, one residue (I419) in strand A, two residues (I462 and K464) in the D strand, and one additional residue (Y442) in the C strand. While most AAVPHP.eB capsid interacting residues of PKD2 reside in the N-terminal, A-B loop and B-C loop, two residues (E418 and I419) in strand A, one residue (Y442) in the C strand, but only one residue (I462) reside in D strand (Tables S2 and S3). Surface plasmon resonance (SPR) measurements indicated that AAV9 binds with AAVR at a equilibrium dissociation constant (KD) of 138.5 nM *in vitro*, whereas the KD of AAVPHP.eB to AAVR was evaluated at 273.8 nM (Figure S6). The narrow interface between AAVPHP.eB and AAVR PKD2 may provide an explanation for the lower affinity of AAVPHP.eB to AAVR at a molecular level.

Capsid structure of AAV9 and AAVPHP.eB upon AAVR binding

Consistent with previously reported AAV structures, only viral protein (VP) 3 common region density can be defined in AAV9 and AAVPHP.eB reconstruction maps. For AAV9, amino acid density from D219 to L736 was observable, and for AAVPHP.eB amino acid density from D219 to L743 was observable. In AAV9, there were 12 capsomer A residues and 4 capsomer B residues within 4 Å distance of AAVR PKD2 (Table S2). In AAVPHP.eB, 13 capsomer A residues and 5 capsomer B residues were within 4 Å distance of AAVR PKD2 (Table S2). All capsid residues close to AAVR PKD2 in both AAV9 and AAVPHP.eB reside in VR-I, VR-III, VR-IV, VR-V, and VR-VIII.

The main-chain density of VR-VIII in AAV9 prior to and post AAVR binding can be well defined at SD level of 1.5 (Figures 3A and 3B). While AAVPHP.eB possessed an engineered VR-VIII with an insertion of seven peptides (TLAVPFK) between the residue 588 and 589 and two mutations (A587D, Q588G in AAVPHP.eB numbering).[7] The seven-amino-acid insertion pointed further out from the capsid and does not alter the conformation of the ascending arm before S586 and descending arm after A596. The density of residues that reside at the base of the native AAVPHP.eB VR-VIII insertion was evident at SD level of 0.65, but L590 and A591, which reside on the top of the engineered loop still lack density under the same SD level (Figure 3C). Compared with the recently reported AAVPHP.B VR-VIII structure (main chain of S587–T589 and P593–F594 could be fitted into density),[18] the main-chain position of the engineered VR-VIII in our native AAVPHP.eB structure could be better defined. Upon AAVR

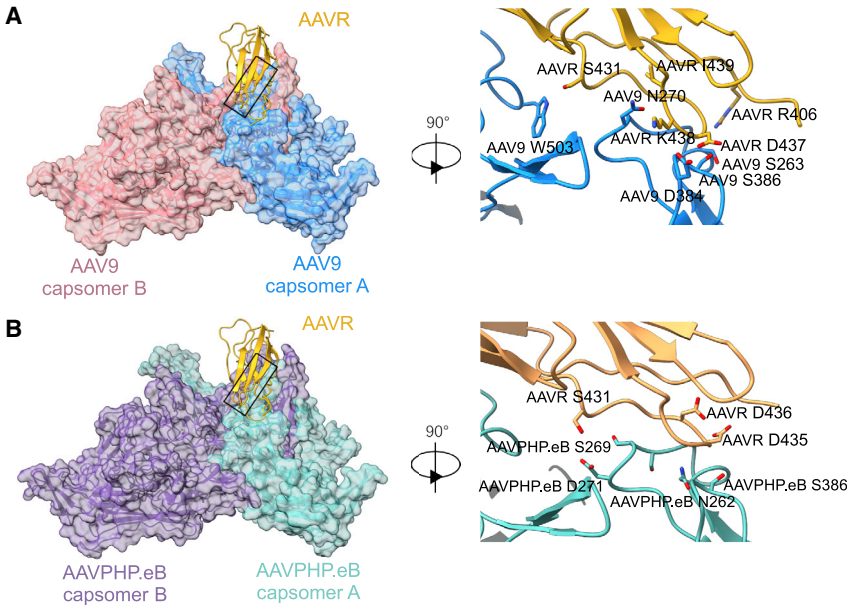

Figure 2. receptor interface of AAV9-AAVR and AAVPHP.eB-AAVR complexes

(A) One AAVR PKD2 (gold) interacts with two AAV9 capsomers (blue indication capsomer A, pink indicating capsomer B), and close-up view of the boxed region (90° rotation around Y axis). Only residues have potential interactions are labeled in the diagram. (B). One AAVR PKD2 (gold) interacts with two AAVPHP.eB capsomers (turquoise indicating capsomer A, purple indicating capsomer B), and close-up view of the boxed region (90° rotation around Y axis).

binding, the main-chain density of L590 and A591 was revealed at SD level of 0.65 and the VR-VIII density can be better defined (Figure 3D). The main-chain density of other AAVR PKD2 interacting VRs (VR-I, VR-III, VR-IV, and VR-V) in AAV9 and AAVPHP.eB native or AAVR bound state can be defined at SD level of 1 (Figures S4 and S5).

Both AAV9 and AAVPHP.eB capsid protein showed negligible overall conformational change upon AAVR binding. The capsid structures of native AAV9 and AAV9 complexed with AAVR shared a root-mean-square deviation (RMSD) of 0.480 across all Cα atoms in 518 residues, and the capsid structures of AAVPHP.eB and AAVPHP.eB complexed with AAVR differed by an RMSD of 0.515 across all Cα atoms in 527 residues.

In previous studies, S268 located in AAVrh.10 VR-I was proposed to be a key residue in BBB penetration.[19,20] Interestingly, S268 is also conserved in the AAV9 and AAVPHP.eB sequence (Figure S9). However, the VR-Is in AAV9 and AAVPHP.eB had modest densities regardless of AAVR binding, with only main-chain densities evident at SD levels of 1.5 or lower (Figures S4A, S4B, S5A, and S5B). Recent structural study of AAV9-glactose suggested that binding of galactose could stabilize the conformation of VR-I.[15] Collectively, VR-I demonstrated a multiple-receptors engagement behavior that might be the underlying reason for AAV9 and AAVPHP.eB special tropism.

Diverse VR conformation in various AAV serotypes

To characterize similarities and differences between AAVR PKD2 interacting and BBB penetrating AAVs, we superposed AAV1, AAV2, AAV9, AAVPHP.eB, and AAVrh.10 capsid structures. Superposition suggested that most structural variability occurred in VR-I, VR-II, VR-IV, and VR-VIII (Figure 4).

AAVR PKD2 interacting VR-I and VR-IV showed most structural diversity among serotypes. Compared with AAV2 VR-I, AAV1 and AAV9/PHP.eB VR-I exhibited more extended loop toward the virus surface due to a single amino acid insertion in AAV1 VR-I and a two-amino-acid insertion in AAV9/PHP.eB. Despite high sequence conservation among AAVrh.10 and AAV9/PHP.eB VR-I (Figure S8), AAVrh.10 VR-I exhibited a different conformation, which pointed outward from the virus surface.

Among AAVR PKD2 interacting AAVs, only AAV9/PHP.eB have potential VR-IV interaction with AAVR. AAV9/PHP.eB VR-IV was closer to adjacent AAVR compared with that of AAV1. AAV2 VR-IV adopted a perpendicular position and more extended conformation compared with that of AAV1 and AAV9/PHP.eB. AAVrh.10 VR-IV had a similar loop conformation to that of AAV1. VR-IIs located around 5-fold axis also exhibit structural discrepancy among serotypes. Of note, although VR-II amino acids are identical in AAV9 and AAVPHP.eB, loops showed different conformation (Figure S8).

Despite the seven-amino-acid insertion and two mutations in VR-VIII of AAVPHP.eB, VR-VIIIs among different AAV serotypes shared common morphology (Figures 4 and S8).

Relationship between AAV9 receptors and neutralizing antibody

Previous studies have identified galactose as a primary attachment receptor for AAV9 and mapped N470, D271, N272, Y446, and W503 as the binding pocket at the region in between 3-fold protrusion and 2/5-fold wall.[21,22] The AAVR PKD2 footprint bridges the 3-fold protrusion and 2/5-fold wall on AAV9/PHP.eB capsid (Figures 5A and 5B). The AAVR PKD2 footprint and galactose binding pocket only share one common residue, W503, indicating galactose and AAVR may serve as independent receptor for AAV9 attachment and transduction.

To date, two antibody-AAV9 complex structures have been reported, including a BALB/c mouse originated, hybridoma-screened antibody PAV9.1 and a commercially available CaptureSelect™ AAV9 Ligand

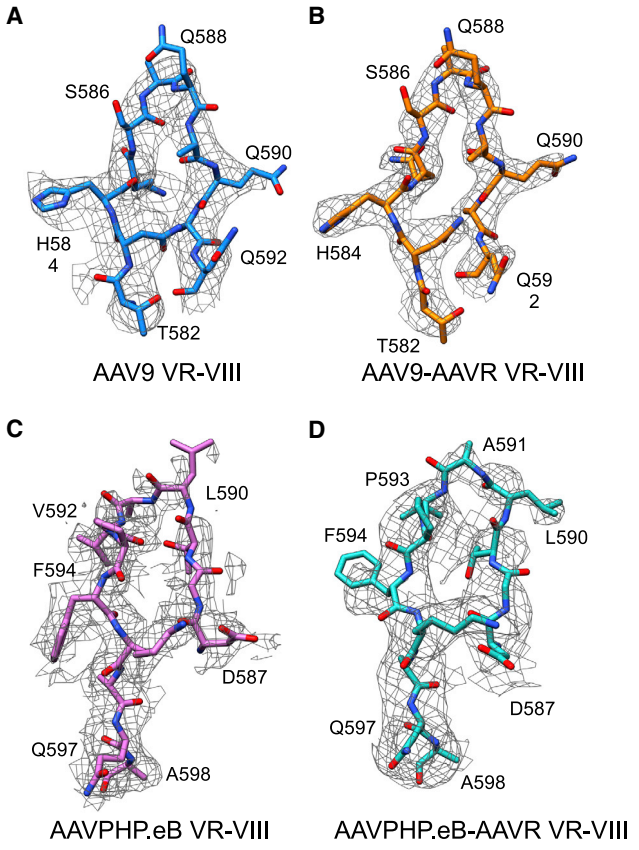

Figure 3. Density maps of VR-VIII

(A) AAV9 (SD level = 1.25), (B) AAV9-AAVR (SD level = 1.5), (C) AAVPHP.eB (SD level = 0.65), and (D) AAVPHP.eB-AAVR (SD level = 0.65) VR-VIII models fitted into density maps. Electron density maps are shown in gray meshes.

(CSAL9), both of which exhibit neutralizing activity against AAV9.[23,24] The epitope of PAV9.1 lies on the 3-fold axis of AAV9, overlapping with AAVR footprint by two residues (Q588 and Q590) (Figure 5C). Another study powered by M13 phage display technology characterized that potential immunogenic AAV9 VP3 epitopes largely overlap with the AAVR footprint regions on 3-fold protrusion and 2/5-fold wall[25] (Figure 5C).

Interestingly, both AAVR PKD2 footprint and epitopes screened from phage display technology only overlap with galactose binding pocket by one residue (W503) on AAV9 capsid (Figure 5C). Again, indicating W503 may serve as important dual functional residue in both galactose-mediated viral attachment and AAVR-mediated transduction. This is also consistent with the finding in a previous mutagenesis study that suggested a dual role of residues from E500 to W503 facilitating successful transduction other than galactose attachment.[26]

Of note, CSAL9 binding to AAV9 occludes residues around the 5-fold axis, and phage display screened epitopes also elicited antigenic VP1/2 N-terminal residues[24,25] (Figure 5C), suggesting that other than AAVR interacting, VP1/2 common N-terminal region may also play crucial role in AAV transduction process.

LY6A binding to AAVPHP.eB

Recent studies have reported that the enhanced CNS transduction and BBB penetration of AAVPHP.eB is driven by a GPI-anchored protein, LY6A, independent of AAVR. We then purified extracellular domain of LY6A fused with monomeric superfolder GFP (msfGFP)[27] to maintain its proper folding in 293F cells. To further investigate AAVPHP.eB and LY6A interaction, SPR sensorgrams revealed a small-molecule-like fast association and disassociation of LY6A to AAVPHP.eB (Figure 6B). While injecting LY6A onto the AAV9 immobilized CM5 sensor chip, no SPR signals were detected (Figure 6A). Due to the dynamic interaction of LY6A to AAVPHP.eB, we incubated LY6A and AAVPHP.eB in the absence of AAVR with glutaraldehyde (at a final concentration of 0.05%) immediately before applying to cryo-sample grids. Then the preliminary structure of AAVPHP.eB-LY6A was characterized by cryo-EM at 200 kV. An additional vague density is observed on the top of AAVPHP.eB 3-fold axis and did not occupy the binding position of AAVR PKD2 (Figures 1D and 6C). To further validate the LY6A binding site on AAVPHP.eB, an SPR competition assay was performed. Competitive binding should result in negligible change in binding response between two purified receptors injections, whereas non-competitive binding is expected to produce an additive/cumulative binding response. Analysis of the resultant sensorgrams showed that the binding of AAVR had no impact on subsequent LY6A binding and vice versa (Figure S6). Additionally, the density extended from the middle of the 3-fold axis to interact with 3-fold protrusion formed by VR-VIII (Figures 6D and 6E). These findings further demonstrated that the newly identified receptor LY6A is responsible for directly interacting with AAVPHP.eB with distinctive binding sites independent of AAVR.

DISCUSSION

In this study, we reported the native AAV9 and AAVPHP.eB and their complex structures with cellular receptor AAVR. The structures of AAV9-AAVR and AAVPHP.eB-AAVR demonstrate that AAVR PKD2 binds to AAV9/PHP.eB between 3-fold protrusion and 2/5-fold wall, which shared a similar AAVR interaction pattern with that of AAV1 and AAV2.

VR-I, VR-III, VR-IV, VR-V, and VR-VIII in AAV9 and AAVPHP.eB engaged with AAVR PKD2, which differ from AAVR PKD2 interacting VRs in AAV1 and AAV2 by VR-IV and VR-V. VR-IVs exhibit most conformational variance in AAV9/PHP.eB. VR-IVs are spatially closer in distance to adjacent AAVR to facilitate interaction among PKD2 interacting AAV serotypes. Despite common morphology among VR-Vs in different AAV serotypes, E500 and W503 in AAV9 VR-V have potential contacts with AAVR PKD2. Of note, W503 also plays a role in galactose binding in AAV9. Our structural finding further supports the notion that E500-W503 in the AAV9 capsid possess dual function for galactose binding and the virus post-attachment process in a previous study.[26]

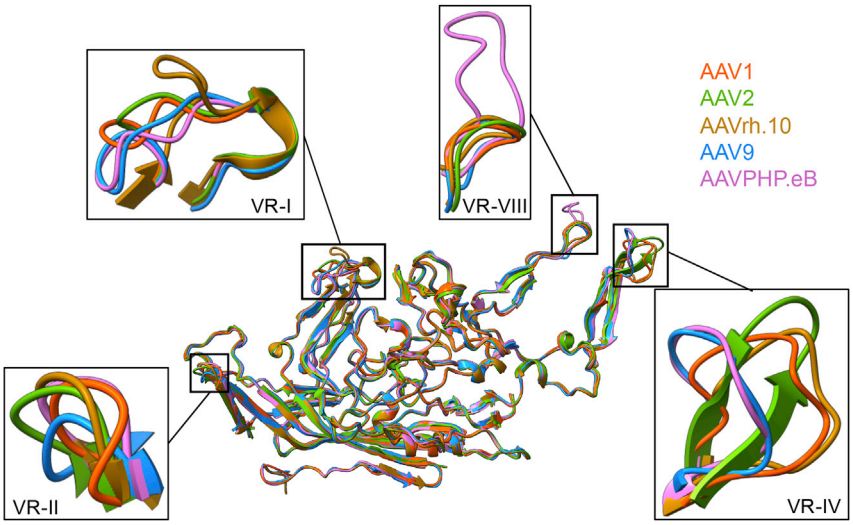

Figure 4. Structural superposition of VPs
Superposition of VP structures from AAV1, 2, 9, PHP.eB, and rh.10. Black boxes indicate the enlarged VR-I, VR-II, VR-IV, and VR-VIII.

The hybridoma-screened antibody PAV9.1 epitope footprint slightly overlaps with that of AAVR PKD2 on AAV9 (Q588 and Q590), and the immunogenetic peptides screened by phage display technique exhibit large overlap with AAVR PKD2 footprint on AAV9 VR-III and VR-V. This result indicates one potential antibody neutralizing mechanism is to occlude AAVR binding and virus cellular trafficking. However, another commercial ligand CASL9 epitope resides around the AAV9 5-fold axis, and the phage display screened immunogenetic peptides also suggest VP1 unique and VP1/2 common regions are antigenic, suggesting the alternative neutralizing mechanism through interfering with the AAV9 cellular trafficking process other than AAVR binding.

AAV9 and its engineered variant AAVPHP.eB support the transduction of CNS and are able to cross the BBB. However, little difference in AAV9 and AAVPHP.eB capsids upon AAVR interaction was observed, including the engineered VR-VIII in AAVPHP.eB, and S268 containing VR-Is have modest densities in both AAV9 and AAVPHP.eB regardless of AAVR binding. Recent study elucidated that AAVR interacting VR-I also participates in AAV9 galactose binding and might have been selected during evolution to ensure the virus internalization;[15] this is in line with the role of AAVR facilitating intracellular trafficking of the virus.[9,28]

In the light of studies on newly acquired LY6A binding ability of AAVPHP.eB, we tried to further explore the molecular basis of AAVPHP.eB interaction with LY6A. We found that LY6A interact with AAVPHP.eB independent of AAVR and the engineered VR-VIII in AAVPHP.eB had potential interaction with LY6A, suggesting engineered VR-VIII facilitated the alternative receptor recognition ability for AAVPHP.eB.

In summary, the structures of neurotropic clade F AAV9 and its engineered variant AAVPHP.eB in complex with AAVR deepened the understanding of AAV receptor engagement and one dominant neutralizing mechanism. Structural analysis of AAV9-AAVR and AAVPHP.eB-AAVR suggest VR-I and VR-V may play an interesting role in virus transduction through multiple receptor engagement. Structure information of AAVPHP.eB-LY6A also indicated that the enhanced CNS transducing character is also facilitated by novel receptor LY6A recognition independent of AAVR. These results reiterate the conclusion drawn in a recent study that enhanced BBB-crossing character of AAVPHP.eB might be determined by multiple factors.[18] Our structure information may provide more insights for AAV vector engineering in attempts for higher transduction efficiency and altered tissue tropism.

MATERIALS AND METHODS

Virus production and purification

Triple-plasmid transfection using polyethylenimine reagent (PEIMAX) (no. 24765, Polysciences, USA) was carried out to produce recombinant AAV9 and AAVPHP.eB according to a previously reported procedure with modifications.[11,14] Briefly, the plasmids pAAV9-GFP or pAAVPHP.eB-GFP; pRepCap with AAV9 or AAVPHP.eB encoding the Rep and Cap proteins; and pHelper plasmids were co-transfected into HEK293T cells. Cells were harvested 72 h post transfection, then AAVs were purified with iodixanol gradient centrifugation. AAV genome copy titers were determined by real-time quantitative PCR (qPCR) using primers specific for the GFP gene sequences. The primers used were as follows: qpcr-GFP-F, TCTTCAAGTCCGCCATGCC; qpcr-GFP-R, TGTCGCCCTCGAACTTCAC.

Purification of AAVR proteins

cDNAs encoding the AAVR PKD1-5 domains with a C-terminal His-tag in a pET28a vector were transformed into *Escherichia coli* BL21 (DE3) cells harboring the recombinant plasmids and were cultured in Luria-Bertani (LB) medium containing 50 μg/mL kanamycin at 37°C. Protein expression was induced by the addition of isopropyl 0.5 mM β-D-thiogalactoside (IPTG) at the optical density 600 (OD600) of 0.6, followed by another 16 h of cell culture. Protein purification was performed according to the previous reports.[11,14] Briefly, recombinant protein was first purified by nickel affinity chromatography (Qiagen, Holland), then further purified by size exclusion using Superdex 200 increase (GE Healthcare, USA). Size-exclusion fractions were collected starting around 14 ml. The purified proteins were concentrated to 6 mg/mL for storage at −80 °C.

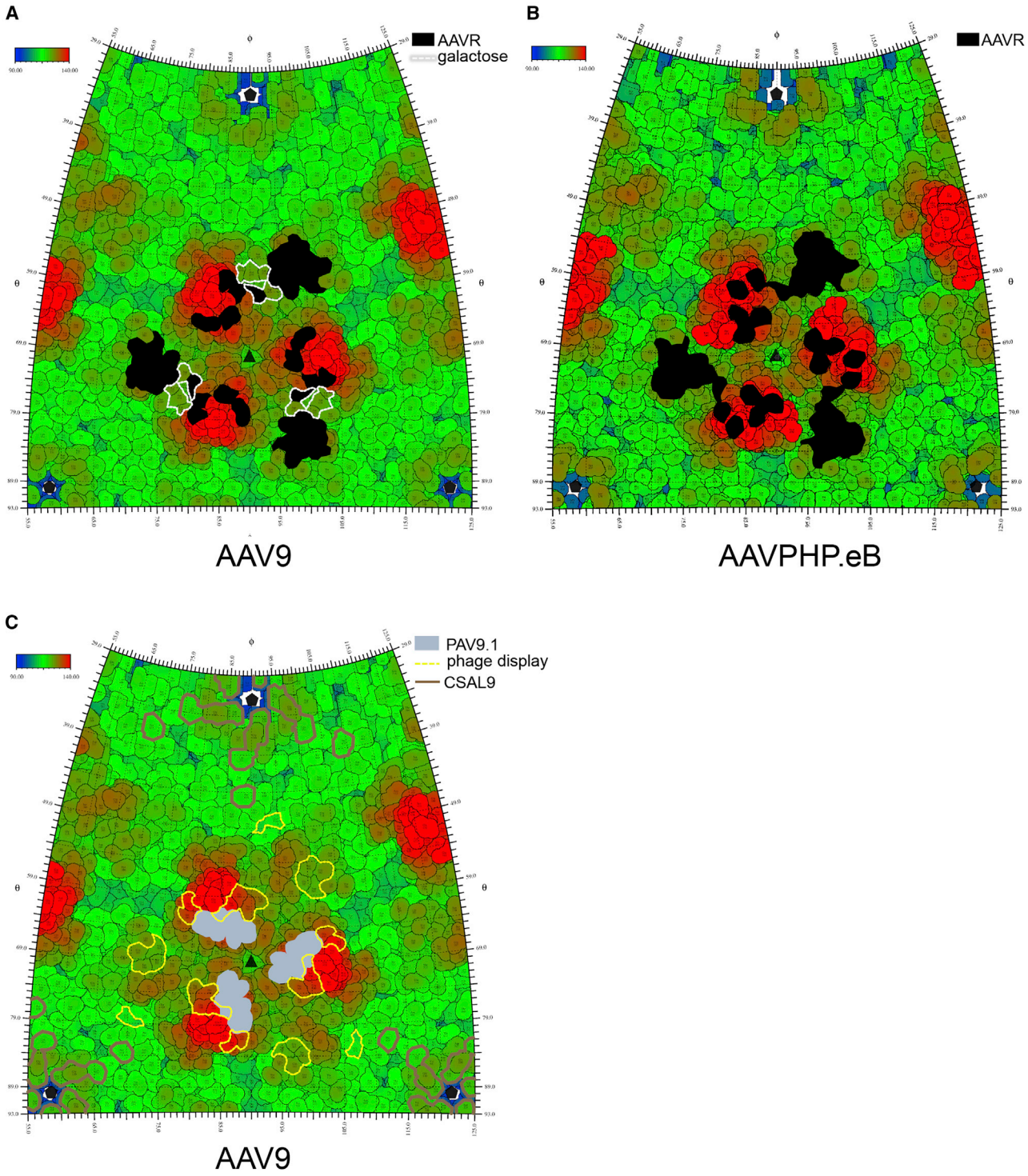

Figure 5. Receptor and antibody binding footprint on AAV9 and AAVPHP.eB capsid

Projections of the AAV9 and AAVPHP.eB surface. In (A) AAV9, AAVR PKD2 footprint is filled in black and galactose footprint is outlined in white. On (B) AAVPHP.eB, AAVR PKD2 footprints are filled in black. On (C) AAV9, PAV9.1 footprints are filled in gray and phage display screened immunogenetic peptides are outlined in yellow dashed lines. CSAL9 epitopes are outlined in brown lines. Roadmaps was generated by RIVEM, and the two angles (θ, φ) define a vector and a further location on the icosahedron surface. As shown by the key, roadmaps are colored by distance from the center of the virus from blue (radius = 90Å) to red (radius = 140Å).

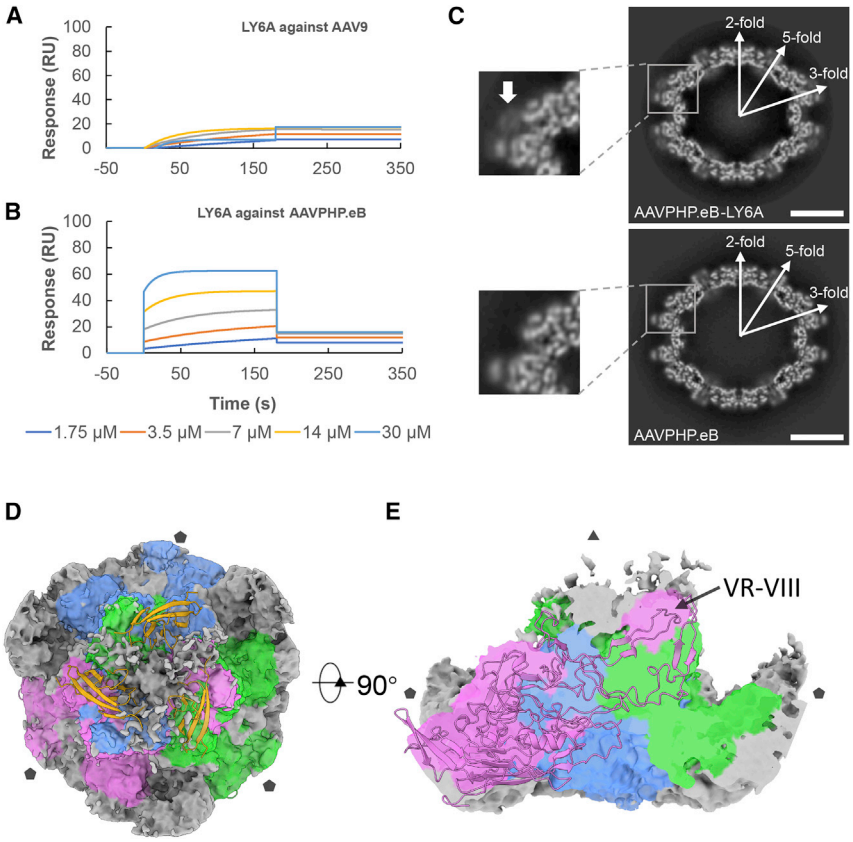

Figure 6. LY6A binding to AAVPHP.eB

SPR sensorgrams for binding of LY6A as analyte to immobilized (A) AAV9 and (B) AAVPHP.eB on CM5 chip. (C) central cross sections through the cryo-EM map of AAVPHP.eB-LY6A (upper part) and native AAVPHP.eB (lower part). Arrow indicates the additional density above 3-fold axis. The scale bars represent 100 Å. (D) Top view of the AAVPHP.eB-LY6A complex 3-fold axis density. An AAVPHP.eB capsid trimer model was fitted into density and 5.5 Å threshold was used to color density around AAVPHP.eB capsomer A, B, and C models into blue, green, and pink, respectively. Gray parts indicate densities which were beyond 5.5 Å to AAVPHP.eB capsid trimer model. Three ribbon models of AAVR PKD2 domains (golden) are presented at the theoretical binding positions on AAVPHP.eB capsid to indicate the additional LY6A density (gray densities on top of 3-fold axis) relative to AAVR PKD2 binding site. (E) is the 90° X axis rotation and side view section of (D), an AAVPHP.eB capsomer C ribbon model (pink) was fitted into the corresponding position in density to indicate the position of engineered VR-VIII relative to LY6A density (gray densities on top of 3-fold axis). Icosahedral 3-fold axis and 5-fold axis are represented by black triangles and pentagons, respectively.

Sample preparation and cryo-EM data collection

AAV9 or AAVPHP.eB particles and purified wild-type AAVR were mixed at a molar ratio of 1:120 (AAV:AAVR) at 4°C for 1 h. An aliquot of 3 μL of each mixture was loaded onto a glow-discharged, carbon-coated copper grid (GIG, Au 2/1 200 mesh; Lantuo, China) bearing an ultrathin layer of carbon. The grid was then blotted for 4.5 s with a blot force of 0 in 100% relative humidity and plunge frozen in liquid ethane using a Vitrobot Mark IV (FEI, USA). Cryo-EM data were collected with a 200 kV Arctica D683 electron microscope (FEI, USA) and a Falcon II direct electron detector (FEI, USA). A series of micrographs were collected as movies (19 frames, 1.2 s) and recorded with −2.2 to −0.5-μm defocus at a calibrated magnification of 110,000×, resulting in a pixel size of 0.93 Å per pixel. Statistics for data collection and refinement are summarized in Table S1.

Image processing and three-dimensional reconstruction

Similar image processing procedures were employed for all datasets. Individual frames from each micrograph movie were aligned and averaged using MotionCor2[29] to produce drift-corrected images. Particles were picked and selected in RELION 2.1,[30] and the contrast transfer function (CTF) parameters were estimated using CTFFIND4.[31] Subsequent steps for particle picking and two-dimensional (2D) and three-dimensional (3D) classification were performed with RELION 2.1. The final selected particles (for AAVR complex samples, particles in the 3D classes that generated averages showing additional density above the viral capsid were for further reconstruction) were reconstructed with THUNDER.[32] For all reconstructions, the final resolution was assessed using the gold-standard FSC criterion (FSC = 0.143) with RELION 2.1.

Model building and refinement

To solve the structure of AAV9 and AAVPHP.eB, the X-ray crystal structure of AAV9 (PDB: 3UX1)[14] was manually placed and rigid body fitted into the cryo-EM density map with UCSF Chimera.[33] To solve the AAV9-AAVR and AAVPHP.eB-AAVR complexes, the PKD2 domain structure from the AAV2-AAVR structure (PDB: 6IHB) was manually aligned with cryo-EM density corresponding to the bound receptors. Manual adjustment of amino acids of AAV9/PHP.eB and PKD2 was performed using Coot[34] in combination with real space refinement with Phenix. The data validation statistics shown in Table S1 were reported by MolProbity using the integrated function within the Phenix statistics module.[35]

SPR

SPR analyses were carried out using a Biacore T200 (GE Healthcare, USA) with a flow rate of 30 μL/min at 25°C in PBS buffer. AAV9 or AAVPHP.eB particles suspended in sodium acetate buffer (pH 4.0) were immobilized on a CM5 sensor chip by amide coupling. Different concentrations of the recombinant wild-type AAVR protein flowed over the chip and glycine-HCl (10 mM glycine, pH 2.0) were used for chip surface regeneration. The binding affinity was determined by BIAEvaluation software (GE Healthcare, USA).

SPR binding competition assay

Binding competition assays were performed by SPR (Biacore S200, GE). A-B-A injection method was used to unravel if LY6A and AAVR will simultaneously bind to AAVPHP.eB capsid. The AAVPHP.eB capsid was immobilized as described above. The A-B-A injection method was used with 90s injections of analyte A to ensure saturation or near-saturation was reached prior to injection of analyte B. Then analyte B was injected with saturated concentration of first analyte A presence.

Data availability

The cryo-EM density maps and the structures were deposited into the Electron Microscopy DataBank (EMDB) and PDB with the following accession numbers: AAV9 alone (PDB: 7WJW); AAV9-AAVR (PDB: 7WJX); AAVPHP.eB alone (PDB: 7WQO); and AAVPHP.eB-AAVR (PDB: 7WQP). All other data supporting the findings of this study are available from the corresponding authors upon request.

SUPPLEMENTAL INFORMATION

Supplemental information can be found online at https://doi.org/10.1016/j.omtm.2022.05.009.

ACKNOWLEDGMENTS

We thank the computing and cryo-EM platforms of Tsinghua University, Branch of the National Center for Protein Sciences (Beijing) for providing facilities. We thank Dr. Jianlin Lei and Mr. Tao Liu for their help in data collection. This work was supported by the National Natural Science Foundation of China (grant no. 31971126 and U20A20135), the National Program on Key Research Project of China (2020YFA0707500 and 2017YFC0840300), the China Postdoctoral Science Foundation (Grant BX2021165), and the Shuimu Tsinghua Scholar Program of Tsinghua University (Grant 2020SM142).

AUTHOR CONTRIBUTIONS

Z.L. and G.X. conceived the project. G.X., R.Z., and Z.L. designed the experiments. G.X., R.Z., K.Y., and X.M performed experiments. G.X., R.Z., and Z.L. analyzed the data. Z.L. and G.X. wrote the manuscript. All authors discussed the experiments, and read and approved the manuscript.

DECLARATION OF INTERESTS

The authors declare no competing interests.

REFERENCES

1. Melchiorri, D., Pani, L., Gasparini, P., Cossu, G., Ancans, J., Borg, J.J., Drai, C., Fiedor, P., Flory, E., Hudson, I., et al. (2013). Regulatory evaluation of Glybera in Europe — two committees, one mission. Nat. Rev. Drug Discov. *12*, 719. https://doi.org/10.1038/nrd3835-c1.

2. Russell, S., Bennett, J., Wellman, J.A., Chung, D.C., Yu, Z.-F., Tillman, A., Wittes, J., Pappas, J., Elci, O., McCague, S., et al. (2017). Efficacy and safety of voretigene neparvovec (AAV2-hRPE65v2) in patients with RPE65 -mediated inherited retinal dystrophy: a randomised, controlled, open-label, phase 3 trial. Lancet *390*, 849–860. https://doi.org/10.1016/s0140-6736(17)31868-8.

3. Al-Zaidy, S., Pickard, A.S., Kotha, K., Alfano, L.N., Lowes, L., Paul, G., Church, K., Lehman, K., Sproule, D.M., Dabbous, O., et al. (2019). Health outcomes in spinal muscular atrophy type 1 following AVXS-101 gene replacement therapy. Pediatr. Pulmonol. *54*, 179–185. https://doi.org/10.1002/ppul.24203.

4. Wu, Z., Asokan, A., and Samulski, R.J. (2006). Adeno-associated virus serotypes: vector toolkit for human gene therapy. Mol. Ther. *14*, 316–327. https://doi.org/10.1016/j.ymthe.2006.05.009.

5. Terstappen, G.C., Meyer, A.H., Bell, R.D., and Zhang, W. (2021). Strategies for delivering therapeutics across the blood–brain barrier. Nat. Rev. Drug Discov. *20*, 362–383. https://doi.org/10.1038/s41573-021-00139-y.

6. Deverman, B.E., Pravdo, P.L., Simpson, B.P., Kumar, S.R., Chan, K.Y., Banerjee, A., Wu, W.-L., Yang, B., Huber, N., Pasca, S.P., and Gradinaru, V. (2016). Cre-dependent selection yields AAV variants for widespread gene transfer to the adult brain. Nat. Biotechnol. *34*, 204–209. https://doi.org/10.1038/nbt.3440.

7. Chan, K.Y., Jang, M.J., Yoo, B.B., Greenbaum, A., Ravi, N., Wu, W.-L., Sánchez-Guardado, L., Lois, C., Mazmanian, S.K., Deverman, B.E., and Gradinaru, V. (2017). Engineered AAVs for efficient noninvasive gene delivery to the central and peripheral nervous systems. Nat. Neurosci. *20*, 1172–1179. https://doi.org/10.1038/nn.4593.

8. Ravindra Kumar, S., Miles, T.F., Chen, X., Brown, D., Dobreva, T., Huang, Q., Ding, X., Luo, Y., Einarsson, P.H., Greenbaum, A., et al. (2020). Multiplexed Cre-dependent selection yields systemic AAVs for targeting distinct brain cell types. Nat. Methods *17*, 541–550. https://doi.org/10.1038/s41592-020-0799-7.

9. Pillay, S., Meyer, N.L., Puschnik, A.S., Davulcu, O., Diep, J., Ishikawa, Y., Jae, L.T., Wosen, J.E., Nagamine, C.M., Chapman, M.S., and Carette, J.E. (2016). An essential receptor for adeno-associated virus infection. Nature *530*, 108–112. https://doi.org/10.1038/nature16465.

10. Pillay, S., Zou, W., Cheng, F., Puschnik, A.S., Meyer, N.L., Ganaie, S.S., Deng, X., Wosen, J.E., Davulcu, O., Yan, Z., et al. (2017). Adeno-associated virus (AAV) serotypes have distinctive interactions with domains of the cellular AAV receptor. J. Virol. *91*, e00391-17. /jvi/91/18/e00391-17.atom. https://doi.org/10.1128/jvi.00391-17.

11. Zhang, R., Xu, G., Cao, L., Sun, Z., He, Y., Cui, M., Sun, Y., Li, S., Li, H., Qin, L., et al. (2019). Divergent engagements between adeno-associated viruses with their cellular receptor AAVR. Nat. Commun. *10*, 3760. https://doi.org/10.1038/s41467-019-11668-x.

12. Huang, Q., Chan, K.Y., Tobey, I.G., Chan, Y.A., Poterba, T., Boutros, C.L., Balazs, A.B., Daneman, R., Bloom, J.M., Seed, C., and Deverman, B.E. (2019). Delivering genes across the blood-brain barrier: LY6A, a novel cellular receptor for AAV-PHP.B capsids. PLoS One *14*, e0225206. https://doi.org/10.1371/journal.pone.0225206.

13. Hordeaux, J., Yuan, Y., Clark, P.M., Wang, Q., Martino, R.A., Sims, J.J., Bell, P., Raymond, A., Stanford, W.L., and Wilson, J.M. (2019). The GPI-linked protein LY6A drives AAV-PHP.B transport across the blood-brain barrier. Mol. Ther. *27*, 912–921. https://doi.org/10.1016/j.ymthe.2019.02.013.

14. DiMattia, M.A., Nam, H.-J., Van Vliet, K., Mitchell, M., Bennett, A., Gurda, B.L., McKenna, R., Olson, N.H., Sinkovits, R.S., Potter, M., et al. (2012). Structural insight into the unique properties of adeno-associated virus serotype 9. J. Virol. *86*, 6947–6958. https://doi.org/10.1128/jvi.07232-11.

15. Penzes, J.J., Chipman, P., Bhattacharya, N., Zeher, A., Huang, R., McKenna, R., and Agbandje-McKenna, M. (2021). Adeno-associated virus 9 structural rearrangements induced by endosomal trafficking pH and glycan attachment. J. Virol. *95*, e0084321. https://doi.org/10.1128/jvi.00843-21.

16. Zhang, R., Cao, L., Cui, M., Sun, Z., Hu, M., Zhang, R., Stuart, W., Zhao, X., Yang, Z., Li, X., et al. (2019). Adeno-associated virus 2 bound to its cellular receptor AAVR. Nat. Microbiol. *4*, 675–682. https://doi.org/10.1038/s41564-018-0356-7.

17. Meyer, N.L., Hu, G., Davulcu, O., Xie, Q., Noble, A.J., Yoshioka, C., Gingerich, D.S., Trzynka, A., David, L., Stagg, S.M., and Chapman, M.S. (2019). Structure of the gene therapy vector, adeno-associated virus with its cell receptor, AAVR. eLife *8*, e44707. https://doi.org/10.7554/elife.44707.

18. Martino, R.A., Fluck, E.C., Murphy, J., Wang, Q., Hoff, H., Pumroy, R.A., Lee, C.Y., Sims, J.J., Roy, S., Moiseenkova-Bell, V.Y., and Wilson, J.M. (2021). Context-specific function of the engineered peptide domain of PHP.B. J. Virol. *95*, e0116421. https://doi.org/10.1128/jvi.01164-21.

19. Albright, B.H., Storey, C.M., Murlidharan, G., Castellanos Rivera, R.M., Berry, G.E., Madigan, V.J., and Asokan, A. (2018). Mapping the structural determinants required for AAVrh.10 transport across the blood-brain barrier. Mol. Ther. *26*, 510–523. https://doi.org/10.1016/j.ymthe.2017.10.017.

20. Mietzsch, M., Barnes, C., Hull, J.A., Chipman, P., Xie, J., Bhattacharya, N., Sousa, D., McKenna, R., Gao, G., and Agbandje-McKenna, M. (2020). Comparative analysis of the capsid structures of AAVrh.10, AAVrh.39, and AAV8. J. Virol. *94*, e01769-19. /jvi/94/6/JVI.01769-19.atom. https://doi.org/10.1128/jvi.01769-19.

21. Shen, S., Bryant, K.D., Brown, S.M., Randell, S.H., and Asokan, A. (2011). Terminal N-Linked galactose is the primary receptor for adeno-associated virus 9. J. Biol. Chem. *286*, 13532–13540. https://doi.org/10.1074/jbc.m110.210922.

22. Bell, C.L., Gurda, B.L., Van Vliet, K., Agbandje-McKenna, M., and Wilson, J.M. (2012). Identification of the galactose binding domain of the adeno-associated virus serotype 9 capsid. J. Virol. *86*, 7326–7333. https://doi.org/10.1128/jvi.00448-12.

23. Giles, A.R., Govindasamy, L., Somanathan, S., and Wilson, J.M. (2018). Mapping an adeno-associated virus 9-specific neutralizing epitope to develop next-generation gene delivery vectors. J. Virol. *92*, e01011-18. /jvi/92/20/e01011-18.atom. https://doi.org/10.1128/jvi.01011-18.

24. Mietzsch, M., Smith, J.K., Yu, J.C., Banala, V., Emmanuel, S.N., Jose, A., Chipman, P., Bhattacharya, N., McKenna, R., and Agbandje-McKenna, M. (2020). Characterization of AAV-specific affinity ligands: consequences for vector purification and development strategies. Mol. Ther. Methods Clin. Dev. *19*, 362–373. https://doi.org/10.1016/j.omtm.2020.10.001.

25. Chew, W.L., Tabebordbar, M., Cheng, J.K.W., Mali, P., Wu, E.Y., Ng, A.H.M., Zhu, K., Wagers, A.J., and Church, G.M. (2016). A multifunctional AAV-CRISPR-Cas9 and its host response. Nat. Methods *13*, 868–874. https://doi.org/10.1038/nmeth.3993.

26. Adachi, K., Enoki, T., Kawano, Y., Veraz, M., and Nakai, H. (2014). Drawing a high-resolution functional map of adeno-associated virus capsid by massively parallel sequencing. Nat. Commun. *5*, 3075. https://doi.org/10.1038/ncomms4075.

27. Pédelacq, J.D., Cabantous, S., Tran, T., Terwilliger, T.C., and Waldo, G.S. (2006). Engineering and characterization of a superfolder green fluorescent protein. Nat. Biotechnol. *24*, 79–88. https://doi.org/10.1038/nbt1172.

28. Dhungel, B.P., Bailey, C.G., and Rasko, J.E.J. (2021). Journey to the center of the cell: tracing the path of AAV transduction. Trends Mol. Med. *27*, 172–184. https://doi.org/10.1016/j.molmed.2020.09.010.

29. Zheng, S.Q., Palovcak, E., Armache, J.-P., Verba, K.A., Cheng, Y., and Agard, D.A. (2017). MotionCor2: anisotropic correction of beam-induced motion for improved cryo-electron microscopy. Nat. Methods *14*, 331–332. https://doi.org/10.1038/nmeth.4193.

30. Scheres, S.H.W. (2012). RELION: implementation of a Bayesian approach to cryo-EM structure determination. J. Struct. Biol. *180*, 519–530. https://doi.org/10.1016/j.jsb.2012.09.006.

31. Rohou, A., and Grigorieff, N. (2015). CTFFIND4: fast and accurate defocus estimation from electron micrographs. J. Struct. Biol. *192*, 216–221. https://doi.org/10.1016/j.jsb.2015.08.008.

32. Hu, M., Yu, H., Gu, K., Wang, Z., Ruan, H., Wang, K., Ren, S., Li, B., Gan, L., Xu, S., et al. (2018). A particle-filter framework for robust cryo-EM 3D reconstruction. Nat. Methods *15*, 1083–1089. https://doi.org/10.1038/s41592-018-0223-8.

33. Pettersen, E.F., Goddard, T.D., Huang, C.C., Couch, G.S., Greenblatt, D.M., Meng, E.C., and Ferrin, T.E. (2004). UCSF Chimera–A visualization system for exploratory research and analysis. J. Comput. Chem. *25*, 1605–1612. https://doi.org/10.1002/jcc.20084.

34. Emsley, P., Lohkamp, B., Scott, W.G., and Cowtan, K. (2010). Features and development of Coot. Acta Crystallogr. D Biol. Crystallogr. *66*, 486–501. https://doi.org/10.1107/s0907444910007493.

35. Afonine, P.V., Klaholz, B.P., Moriarty, N.W., Poon, B.K., Sobolev, O.V., Terwilliger, T.C., Adams, P.D., and Urzhumtsev, A. (2018). New tools for the analysis and validation of cryo-EM maps and atomic models. Acta Crystallogr. D Struct. Biol. *74*, 814–840. https://doi.org/10.1107/s2059798318009324.